Acta Materialia 155 (2018) 104–116

Contents lists available at ScienceDirect

Acta Materialia

journal homepage: www.elsevier.com/locate/actamat

Full length article

Dislocation-type evolution in quasi-statically compressed polycrystalline nickel

Chaoyi Zhu [a], Tyler Harrington [a], George T. Gray III [b], Kenneth S. Vecchio [a, *]

[a] Department of NanoEngineering, UC San Diego, La Jolla, CA, 92131, United States
[b] Los Alamos National Laboratory, Materials Science and Technology Division, Los Alamos, NM, 87545, United States

ARTICLE INFO

Article history:
Received 17 November 2017
Received in revised form
29 April 2018
Accepted 10 May 2018
Available online 30 May 2018

Keywords:
Geometrically necessary dislocations
Electron backscattered diffraction
Ashby dislocation theory
Statistically stored dislocations

ABSTRACT

The nature of dislocation generation as a function of applied plastic strain in quasi-statically compressed polycrystalline pure nickel has been studied experimentally at ambient temperature. First, to ensure representative datasets of the geometrically-necessary dislocation densities (ρ_{GND}) associated with non-uniform plastic deformation, measurements over large (several millimeter square) areas were made using Hough-based EBSD methods. In addition, the total dislocation density (ρ_T) responsible for the overall work hardening is estimated from the measured flow stress based on Taylor's hardening model. Next, the statistically stored dislocation (SSD) density (ρ_{SSD}) is calculated by subtracting the GND density from the total dislocation density. The results demonstrate that in quasi-statically deformed nickel: i) the measured GND density varies linearly as a function of plastic strain in the range between 0.05 and 0.46; although Ashby's model predicts linearity for GND density evolution over entire range of strains, this study does not cover strains below 0.05; ii) the SSD density increases at a rate much faster than GND density; and iii) the SSD density exceeds the GND density at above 0.09 plastic strain. Both i) and ii) are in agreement with Ashby's prediction, while the magnitudes of GND density (iii) differ from Ashby's model prediction, particularly at large applied strains. Overall, this study enables the interplay of GNDs and SSDs in the hardening of nickel to be gleaned in a quantitative sense. This study illustrates that GNDs are the more important for the strength of polycrystalline metals in the early stages of work hardening, whereas SSDs contribute more to the strength at larger strains. Over the range of strain in this study, work hardening is predominantly through rapid multiplication of SSDs; whereas the GND density is initially higher than SSD density at 0.05 probably due to non-linear evolution of GNDs at low strains (<0.05), which will be the subject of future investigation.

1. Introduction

The generation and storage of defects, such as dislocations, play an important role in work hardening of metals and alloys [1–3]. Due to the presence of deformation gradients that arise through pile-up of geometrically necessary dislocations (GNDs), work hardening of polycrystalline or multi-phase alloys is faster than single crystal or single-phase alloys [4]. Hence, these materials are described as being 'plastically non-homogeneous' [5]. For instance, compressive or tensile tests of polycrystalline samples produces slip on the primary slip system within the interior of the grains, whereas the deformation in the near grain boundary regions activates secondary slip and produces orientation gradients in terms of lattice rotation [6–8]. Due to different numbers of active slip systems or different magnitudes of plastic slip within different regions of a grain, geometrically necessary boundaries (GNBs) are formed, which divide the grain into cell blocks [7,9–11]. GNDs can also reduce their free energy through formation of stable low angle tilt boundaries, which are free of long-range strains and stresses, if Frank's formula is satisfied [12,13]. According to the formulation of Nye, the orientation gradients are accommodated through arrays of GNDs, which generate a lattice curvature K equivalent to the geometrically necessary dislocation density multiplied by the Burgers vector: $\rho_{GND} \cdot b$ [14].

In contrast, homogeneous deformation (i.e. tensile) of pure high stacking fault energy (SFE) face centered cubic (FCC) single crystal metals, where dislocation slip is dominant, does not produce geometrically necessary dislocations, though dislocations do

* Corresponding author.
E-mail address: kvecchio@ucsd.edu (K.S. Vecchio).

https://doi.org/10.1016/j.actamat.2018.05.022
1359-6454/

Nomenclature

$\boldsymbol{\beta^{pl}}$	Plastic distortion tensor
$\boldsymbol{\beta^{el}}$	Elastic distortion tensor
$\boldsymbol{\alpha}$	Nye dislocation tensor
$\boldsymbol{B}$	Local Burgers vector
g	Lattice orientation tensor
$\Delta\varnothing$	Misorientation matrix
$\Delta\varnothing_{,\boldsymbol{l}}$	Lattice orientation gradient in the direction l
b	Burgers vector for slip
$\widehat{\mathbf{l}}$	Dislocation line vector
ρ_{GND}	Geometrically necessary dislocation density
ρ_{SSD}	Statistically stored dislocation density
ρ_{T}	Total dislocation density
γ	Plastic shear strain
λ_{G}	Average slip distance
c	Empirical coefficient
G	Shear modulus
τ_{0}	Lattice frictional stress
τ	Shear stress
σ_{flow}	Flow stress
$\overline{m}$	Taylor's factor

accumulate and contribute to the overall work hardening [14,15]. In this case, these non-geometric dislocations, often present as dipoles or multipoles, are called statically stored dislocations (SSDs), and are generated through a random mutual trapping process [16]. At small scale, on the order of a few micrometers, SSDs organize into heterogeneous mosaic patterns, which consist of dislocation tangles, low-density cells and high-density walls (i.e. incidental dislocation boundaries or IDBs) and microbands [11,17–20]. Moreover, statistically stored dislocations are generated in both plastically homogeneous and non-homogeneous materials during deformation, making an additional contribution to work hardening. In reality, the type of dislocation, either SSD or GND, is a matter of the window size of the measurement. For a small enough window size, every dislocation can be regarded as a GND. The appropriate choice of window size is therefore critical to the determination of an accurate GND density. Jiang et al. [21] point out that a compromise has to be made in order to reduce noise from a window size being too small and avoid GNDs being counted as SSDs when the window size is too large. The reasonable range of step size for GND density characterization is given by Kysar *et al*. [22].

According to Ashby's dislocation evolution model [3], the contribution of GNDs to strength dominates over SSDs in the early stage of work hardening, where the plastic strain is small, but SSDs prevail in the later stages where the strain is large. However, to the knowledge of the present authors, no quantitative experimental evidence has been provided so far to support this statement, which is likely due to a lack of an experimentally viable and quantitative approach that has been developed to estimate the SSD density in the material. Quantitative analysis of SSD density remains challenging since the measurement of dislocations requires a large amount of data across many grains, as well as the spatial gradient in dislocation density within grains, which can be time-consuming and statistically challenging in transmission electron microscopy (TEM)-based techniques. Additionally, it is difficult to isolate SSDs from GNDs unless a fast and reliable method is available for measuring GND density.

Fortunately, with recent advances in the development of the EBSD technique, it is now possible to automate orientation measurement over large regions of interest at a fast frame rate [23–25] and post-process the data to extract the GND density. This technique probes the orientation information from a section/surface of bulk samples at a minimum spatial resolution of 30 nm, which is sufficient to resolve details of dislocation cells/dislocation substructure. For higher resolution of the GND density spatial mapping, transmission Kikuchi diffraction [26] or TEM based precession electron diffraction [27] are typically used. The actual step size of EBSD used for GND calculation is typically greater than the spatial resolution, in order to reduce noise in the measurement, and less than or equal to the size of the dislocation cells [21]. In addition, the degree of pattern binning ranging from 1×1 to 8×8 gives relatively constant average GND density, meaning that the pattern binning is a way of speeding up the data acquisition without compromising the data quality [21]. Due to the nature of EBSD being an in-plane measurement, the full Nye tensor is inaccessible if only 2D EBSD measurements are available, and the necessary assumption has to be made that the lattice orientation gradients in the out-of-plane direction are equal to zero [28]. From the surface misorientation data, the GND density can be calculated using the in-plane Nye tensor. Several methods have been established to obtain the full Nye tensor based on 3D EBSD data using FIB serial cross-sectioning [29–31], neutron diffraction or X-ray micro-diffraction [32,33]. Such measurements are however critical for quantifying GND density in crystallographically or morphologically anisotropic materials [34,35]. For Hough-based EBSD, the noise floor of the calculated GND density is significantly higher compared to HR-EBSD due to poor angular resolution [36]. HR-EBSD is also capable of residual stress and strain measurement, often relative to a chosen reference point within each grain [37]. For GND density measurement, HR-EBSD is a more sensitive technique for small deformations, but the Hough-based method is in general suitable for large deformation cases.

These EBSD-based methods are widely used to extract the part of the dislocation density associated with non-uniform plastic deformation [30,34,35,38,39]. They can also be coupled with digital image correlation and crystal plasticity finite element, shedding light on many aspects of deformation mechanics [40,41]. The present study provides an opportunity to develop a method for determining the SSD density. First, from Taylor's work hardening model, it is assumed that GNDs and SSDs both contribute equally to flow stress. Hence, we are able to estimate, given the flow stress, the total dislocation density (ρ_T) stored in the material due to deformation under quasi-static loading conditions at ambient temperature. Second, the average GND density (ρ_{GND}) can be quantified from EBSD derived orientation data. The difference between the total dislocation density (ρ_T) and GND density (ρ_{GND}) is the SSD density (ρ_{SSD}). It has been shown in this study that we could quantify the SSD density for quasi-statically compressed nickel, and that the attained value is comparable to the measured SSD density in a similar FCC single crystal pure copper from the work of Basinski and Basinski [42].

2. Experimental

The original pure nickel sample was sintered from nickel powder through spark plasma sintering at 1200 °C under a 50 MPa uniaxial load for a 5-min hold. Density was determined via Archimedes in distilled water and shown to be greater than 99% relative density, and no porosity is visible in the microstructure as is evident in Fig. 1b. The sample was characterized with EBSD to reveal the initial microstructure and texture. Six cylindrical compression test samples were electric discharge machined from the sintered piece of pure nickel with dimensions of 3 mm (diameter) by 3 mm (height). Five samples were quasi-statically compressed to various

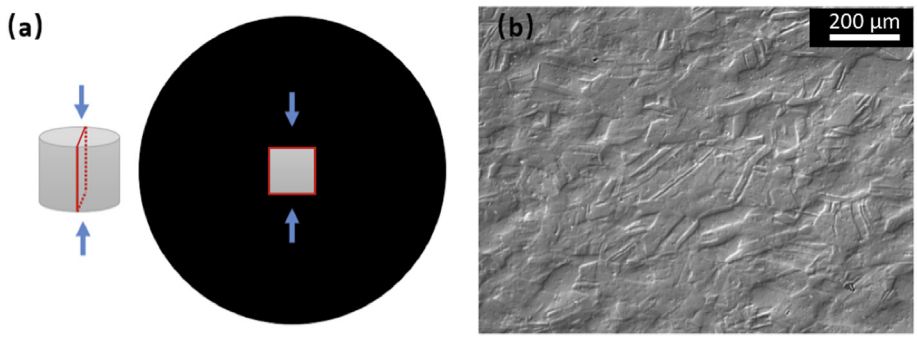

Fig. 1. (a) Schematic diagram showing the mount of the sample with respect to the loading direction (blue arrows) and region of interest (red box); (b) optical micrograph of the polished surface of nickel following 0.33 plastic strain. (For interpretation of the references to colour in this figure legend, the reader is referred to the Web version of this article.)

degrees of deformation using a screw-driven load frame, and their height measured pre- and post-compression via a micrometer. True plastic strain values were calculated from the measured change of height in the samples to be approximately 0.05, 0.11, 0.20, 0.33, and 0.46, respectively for each sample. In addition, the corresponding true flow stress was determined based on the maximum load and current cross-sectional area of the sample to be 289 MPa, 368 MPa, 524 MPa, 651 MPa and 679 MPa, respectively. All the samples were thereafter mounted in conductive resin, and first mechanically ground to the center of the cross section of the sample, as illustrated in Fig. 1a. Next, the samples were polished with 3 μm and 1 μm diamond paste and final polished using a vibratory polisher with 0.05 μm colloidal silica. EBSD was conducted on a Thermo-Fisher (formerly FEI) Apreo SEM at 20 kV equipped with a *Symmetry* EBSD detector from Oxford Instruments at a working distance of ~15 mm. The Oxford *Symmetry* EBSD detector is a new CMOS-based electron backscatter diffraction detector capable of acquiring and indexing greater than 3000 patterns per second. The step size used for the EBSD scan was 500 nm to reveal dislocation cell structures with no binning (1×1). It has been verified in Fig. 12 that 500 nm is a reasonable length scale to characterize GND density, which results in a spread of GND data (green) between the upper and lower limits [22].

Fig. 2 shows the results of the grain size analysis carried out using the number fraction distribution data obtained directly from the Oxford AZtec software. The frequency distribution plot was then fitted with a log-normal distribution and the average grain size, including twins, was calculated to be ~30 μm. Typically, grain size determination does not include twins, as the geometry of twins skew the grain size distribution to the lower end. However, what is of interest in dislocation evolution studies is not the grain size specifically, but the slip distance for dislocations. Twin boundaries can restrict the slip distance for dislocations in a similar manner as grain boundaries and are therefore included in the size analysis. As such, for the remainder of this study, grain size and slip distance can be used interchangeably. In other words, slip distance is defined as the average spacing incorporating both the twin and grain boundaries.

3. Methodology

3.1. GND density calculation based on orientation gradients

The GND density calculation technique utilizes the Nye tensor, computed from the orientation data measured in EBSD. The Nye tensor contains lattice curvature terms that quantify the net dislocation flux through a unit area. In Fig. 3, the surface **S** enclosed by curve **C** contains three dislocation lines of the same sign piercing through the surface.

Using the Stokes' theorem, the line integral of the plastic distortion in the closed surface S can be related to the surface integral of the Nye tensor to obtain the local Burgers vector **B**. This effectively means that the Nye tensor α is a dislocation field tensor.

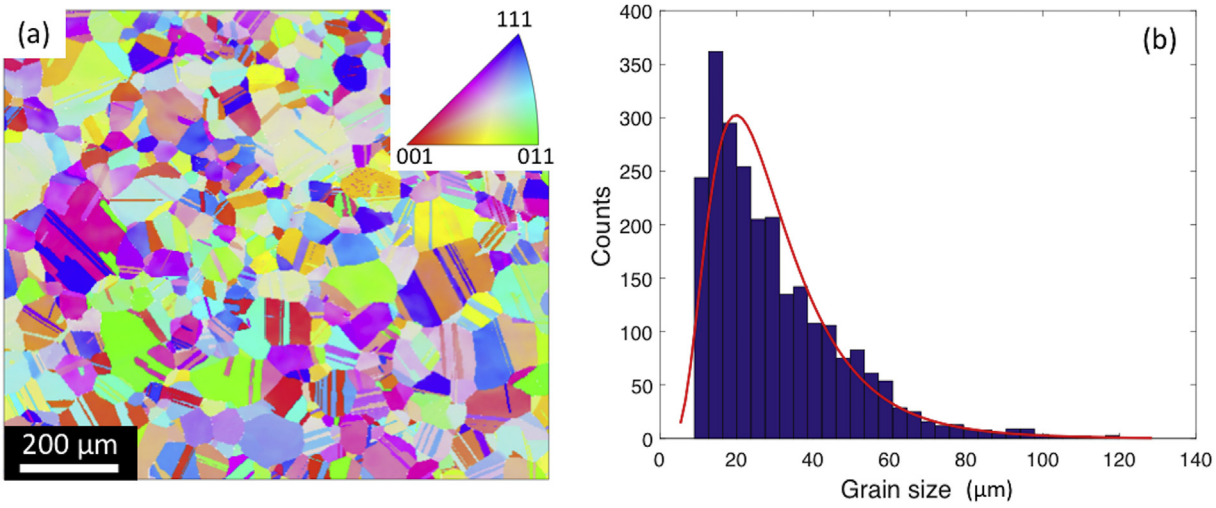

Fig. 2. (a) EBSD image of the undeformed nickel sample plotted with MTEX [58]; (b) Frequency distribution of grain size (blue) including twins fitted with log-normal probability distribution curve (red). (For interpretation of the references to colour in this figure legend, the reader is referred to the Web version of this article.)

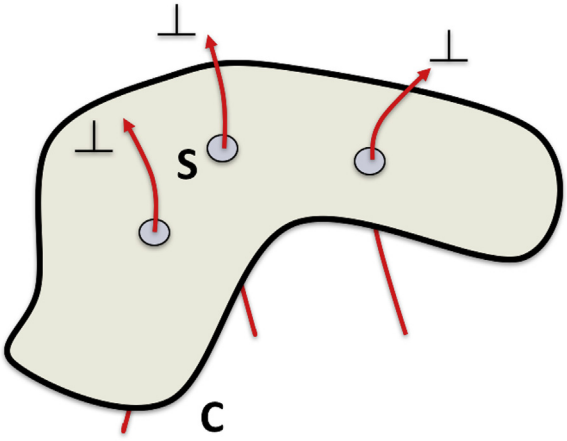

Fig. 3. Schematic of the concept of Nye tensor as dislocation flux through a surface S enclosed by curve C (Adapted from Ref. [31]).

$$\boldsymbol{B} = -\oint \boldsymbol{\beta^{pl}}\boldsymbol{dx} = -\oiint \mathrm{curl}\ \boldsymbol{\beta^{pl}}\boldsymbol{dS} = \oiint \mathrm{curl}\ \boldsymbol{\beta^{el}}\boldsymbol{dS} = \oiint \boldsymbol{\alpha}\boldsymbol{dS} \tag{1}$$

In order to calculate the Nye tensor, the lattice orientation gradients are computed based on the misorientation matrix, $\Delta\varnothing$, i.e. $\Delta\varnothing = g_B g_A^{-1}$. $\Delta\varnothing$ is a tensor that orients the reference point orientation g_A to a point of interest with the orientation matrix g_B. The lattice orientation gradients $\Delta\varnothing_{,l}$ are related to $\Delta\varnothing$ according to Eq. (2), in which d_l is the step size in the direction, l [34]. A detailed derivation of Eq. (2) is given in Appendix A. Symmetry operators are needed in this case to determine the minimum misorientation angle or the disorientation angle $|\Delta\varnothing|$ in order to find the more physically plausible misorientation matrix.

$$\Delta\varnothing_{,l} = \frac{\Delta\varnothing - \mathrm{I}}{d_l} \tag{2}$$

The EBSD technique is employed to measure the lattice orientation gradients and then populate the Nye tensor using Eq. (3). According to Wheeler et al. [57], the Nye dislocation tensor can be represented in different reference frames. Due to small disorientation angles, the error is relatively insignificant, see Appendix B. Additionally, the Nye tensor can also be related to various configurations of dislocations through the Frank's loop construction [12], where $\hat{\mathbf{l}}$ is the dislocation line vector (unit vector), and slip direction is the Burgers vector **b**. This allows computation of the dislocation density of screw and edge dislocations separately. For FCC crystals, there are 6 screw and 12 edge dislocation configurations on the ⟨110⟩{111} slip systems (N = 18) [38].

$$\alpha_{ik} = \varepsilon_{jlk}\frac{\partial \beta_{ij}^{el}}{\partial x_l} \approx \varepsilon_{jlk}\Delta\varnothing_{ij,l} \tag{3}$$

$$\alpha_{ij} = \sum_{n=1}^{N} \rho_{GND}^{n} b_i^n \hat{l}_j^n \tag{4}$$

From Eq. (3) and Eq. (4), the Nye tensor can be rewritten and vectorized as Eq. (5) for the sake of computational simplicity [43]. To solve for the underdetermined system of equations, an appropriate minimization scheme must be chosen. For example, the L^1 energy minimization scheme solves for the dislocation density, i.e. second column of Eq. (5), which minimizes the total elastic energy stored by the dislocations, while still accommodating the measured lattice curvature.

$$\begin{pmatrix} b_1^1 l_1^1 - \frac{1}{2}\boldsymbol{b}^1\cdot\boldsymbol{l}^1, \cdots, b_1^N l_1^N - \frac{1}{2}\boldsymbol{b}^N\cdot\boldsymbol{l}^N \\ b_1^1 l_2^1, \cdots, b_1^N l_2^N \\ b_1^1 l_3^1, \cdots, b_1^N l_3^N \\ b_2^1 l_1^1, \cdots, b_2^N l_1^N \\ b_2^1 l_2^1 - \frac{1}{2}\boldsymbol{b}^1\cdot\boldsymbol{l}^1, \cdots, b_2^N l_2^N - \frac{1}{2}\boldsymbol{b}^N\cdot\boldsymbol{l}^N \\ b_2^1 l_3^1, \cdots, b_2^N l_3^N \end{pmatrix} \begin{pmatrix} \rho_1 \\ \vdots \\ \rho_N \end{pmatrix} = \begin{pmatrix} \frac{1}{2}\boldsymbol{T}(\alpha) - \alpha_{11} \\ -\alpha_{12} \\ -\alpha_{13} \\ -\alpha_{21} \\ \frac{1}{2}\boldsymbol{T}(\alpha) - \alpha_{22} \\ -\alpha_{23} \end{pmatrix} \tag{5}$$

3.2. GND density prediction –Ashby's model

The general form of Ashby's model for GND density, derived from a three-dimensional plate model of a pure polycrystalline or two-phase material is given in Eq. (6) [5]. This expression implies that work hardening due to the presence of GNDs is inversely related to the slip distance.

$$\rho_{GND} = \frac{1}{\lambda_G}\frac{4\gamma}{b} \tag{6}$$

The term λ_G defines the average slip distance of dislocations, i.e. grain size (potentially including twins) or phase separation. In this experiment, the pure nickel sample contains a large fraction of twins due to sintering conditions. Therefore, as previously discussed, grain size here is calculated to include twin boundaries, which also impede the motion of dislocations, in addition to the grain boundaries. To avoid confusion, the term slip distance is used to more accurately reflect the plastic response of the material. γ is the shear strain in the material, which depends on the specific type of active slip system and the grain orientation. For a polycrystalline material, the plastic shear strain in Ashby's model corresponds approximately to 3.06 times the tensile or compressive strain, where 3.06 is the Taylor factor [4]. Using this simple conversion, the original x axis (shear strain) in Ashby's paper has been adapted to plastic strain in Fig. 4.

The average slip distance, λ_G is only dependent on the microstructure of the material. It is generally assumed to be independent of the imposed plastic strain for incompressible materials like metals. Since λ_G, i.e. slip distance, is equivalent to the grain size for an un-twinned, single phase, polycrystalline material, the predicted GND density implies a Hall-Petch type strengthening. On the other hand, the slip distance for SSDs, λ_s, is significantly greater than λ_G, and is dependent on the amount of plastic strain, ranging from 10 μm to 100 μm. According to Ashby's model, GND density varies linearly with respect to the change in the shear strain, γ, but the SSD density increases approximately to the square of shear strain. For materials with a small slip distance (below 100 μm), GND density initially dominates over SSD density for small plastic strains. As plastic strain increases, the slip distance λ_s decreases as work-hardening progresses from Stage I to Stage II. Hence, the density of SSDs increases more dramatically than GNDs, nearly proportional to γ^2. At large deformation, the SSDs overwhelm the GNDs at roughly 0.1 plastic strain according to Ashby's prediction for polycrystalline copper, for a slip distance of approximately 30 μm, see Fig. 4. The yellow region is plotted based on results from Basinski and Basinski [42] for single crystal copper. Since nickel is also an FCC crystal with a lattice parameter nominally similar to that of copper, Fig. 4 should in theory nominally approximate the predicted GND and SSD density for nickel used in this study.

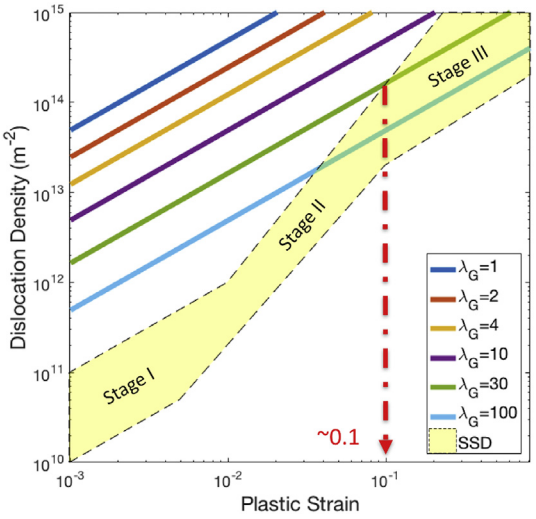

Fig. 4. The predicted GND density and estimated SSD density plotted against plastic strain in polycrystalline pure copper (λ_G is the slip distance with unit of μm) {Adapted from Ashby [5]}. The red dotted arrow points at the predicted plastic strain, at which the SSD density surpasses the GND density for the copper. (For interpretation of the references to colour in this figure legend, the reader is referred to the Web version of this article.)

3.3. Taylor's hardening model

The shear flow stress is related to the dislocation density through Taylor's dislocation model [44]:

$$\tau = \tau_0 + \alpha G\boldsymbol{b}\sqrt{\rho_T} \approx cG\boldsymbol{b}\sqrt{\rho_{GND} + \rho_{SSD}} \tag{7}$$

where the friction stress τ_0 is the resistance to shear when $\rho_T = 0$, which is negligibly small in an FCC crystal [45–47]. The parameter 'c' is the empirical coefficient taken to be ~0.3 [5,48], G is the shear modulus [49] and $\boldsymbol{b}$ is the Burgers vector. Theoretically, c for FCC crystal varies from 0.16 to 1.1 depending on the dislocation type and the type of interaction [48]. However, it is almost impossible to systematically verify the exact degree of contribution of different c values, which also might evolve as dislocations accumulate. Experimentally, the value of c is determined from fitting flow stress and total dislocation density data. In this study, the total dislocation density is unknown. Assuming all the dislocation types and interactions contribute to the hardening listed in Ref. [48], the theoretical contribution of c is estimated to be around 0.3 as well, despite the wide range of variation. The flow stress can then be calculated by multiplying the shear stress by the Taylor factor $\overline{m}$ ($\overline{m} = 3.06$ for FCC crystal), which is an isotropic interpretation of the crystalline anisotropy [4].

$$\sigma_{flow} = \overline{m}\tau = \overline{m}cGb\sqrt{\rho_T} \tag{8}$$

The flow stress can be readily measured during the quasi-static compression test. Having obtained the flow stress, it is possible to calculate the total dislocation density using Eq. (9). Since the ρ_{GND} can be estimated from the Nye tensor, an estimate of the ρ_{SSD} can be obtained through Eq. (10).

$$\rho_T = \frac{\sigma_{flow}^2}{(\overline{m}cGb)^2} \tag{9}$$

$$\rho_{SSD} = \rho_T - \rho_{GND} \tag{10}$$

4. Results

4.1. GND density of quasi-statically compressed nickel

The samples were fabricated to be small so that EBSD scans close to the center of the cross section of sample could approximately characterize the global deformation state. If the sample is too large, the EBSD scan is only a small fraction of the cross section, which may reflect only the local deformation state (non-ideal material deforms more heterogeneously). The samples were made sufficiently small to facilitate characterization of the largest possible area fraction of the compressed material close to the center of the cross-sectional area shown in Fig. 1(a), necessary to extract the majority of GNDs associated with the plastic deformation at the same magnification in the SEM [50]. On the other hand, if the sample is too small, the number of grains may be too limited to achieve statistically valid macroscopic deformation conditions. The EBSD window size in the SEM will be limited by the most deformed sample with 0.46 plastic strain in the compression direction, therefore the final dimension of *this* compressed sample was used to define the EBSD scan area for all samples, with each scan region centered within the sample height. In Fig. 5, it can be seen that the samples for plastic strains less than 0.2 have been indexed successfully without much loss of orientation data. Above 0.2 plastic strain, the pattern degradation due to deformation lowers the fraction of indexed pixels in some regions [51]. Nevertheless, for the most challenging case at 0.46 plastic strain, this sample still has a significant fraction of pixels indexed (~85%), sufficient to carry out the GND density calculation. The Ni microstructure contains annealing twins in the undeformed state, and no evidence of deformation twin activation in the deformed samples, so that all of the plastic strain can be logically attributed principally to dislocation motion and dislocation density evolution.

Following the standard routine for calculating the GND density based on the Nye tensor, it is possible to obtain GND density maps that contain valid GND density data. Several filters have been applied to filter out data: i) below the noise floor of our technique (2.8×10^{13} m^{-2}), ii) overestimated data points sitting on the grain boundary, and iii) data points with disorientation angle below the angular resolution (0.2°) of the instrument. A detailed explanation of the methods used to obtain the noise floor and angular resolution can be found in resource [25]. Following previous works on misorientation distribution measurement [52,53], which describes very similar physical quantities, the GND density data have been fitted with a log-normal probability density function for each sample to evaluate the geometric mean of GND density for each sample.

The log-normal probability density function is:

$$f(x|\,\mu,\sigma) = \frac{1}{x\sigma\sqrt{2\pi}}\exp\left\{\frac{-(\ln x - \mu)^2}{2\sigma^2}\right\} \tag{11}$$

where e^{μ} is the geometric mean and e^{σ} is the geometric standard deviation of the distribution. The geometric standard deviation is then used to plot the error bars for the geometric mean of measured GND density as a measure of dispersion [54]. The upper limit of the error bar is equal to $e^{\mu+\sigma}$, which represents the spread of high density GND structures. The spread of low density GND structure is indicated by the lower limit of the error bar $e^{\mu-\sigma}$. From Fig. 6, the distribution curves start at roughly the same position. It is not surprising to see that the distribution curves shift to higher dislocation densities with increasing plastic strain values and spreads out as the degree of deformation increases the heterogeneity and magnitude of the GND density. Hence, the geometric mean and geometric standard deviation of the GND density both increase with increasing

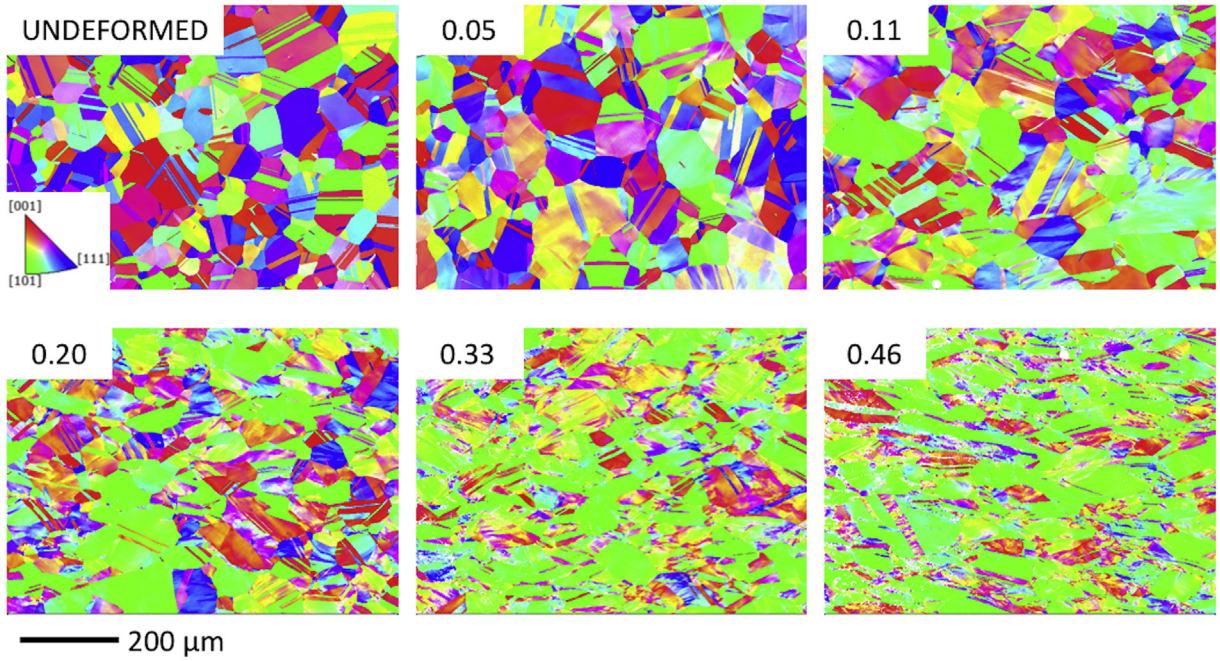

Fig. 5. EBSD images generated from Oxford AZtec software for undeformed nickel and quasi-statically compressed nickel samples at room temperature with plastic strains of 0.05, 0.11, 0.20, 0.33, and 0.46. The 200 μm scale bar applies for all figure segments.

degree of deformation. This agrees well with actual GND density data fitted with lognormal curves in Appendix C. A comparison of the geometric mean value of measured GND density with the predicted result from Ashby's model, shows that they are in good agreement at lower strains, but differ at higher strains. This is demonstrated by the increasing ratio between the GND density predicted by Ashby to the GND density measured by EBSD [3] at increasing strain in Fig. 7a. Fig. 7b shows the measured GND density, represented by the blue line, which varies almost linearly with plastic strain, as does the Ashby's model prediction of GNDs represented by the green line. The magnitude of predicted GND density is within the range of the measured GND density's error bars, but in general slightly higher compared to the measured data. This does not mean that the measured GND density agrees with Ashby's model between 0 and 0.05 strain, which is outside the fitted range in this study. Interpolation of the measured GND density data does not intercept with the origin like Ashby's model prediction, which suggests a rapid multiplication of GNDs below 0.05 strain. Moreover, unlike the predicted result, which monotonically increases with plastic strain, the measured GND density will gradually plateau at higher strain values (>0.5), because significant lattice distortion degrades the pattern quality [51] and eventually results in grain fragmentation. Two further issues regarding the determination of these GND densities should be addressed. The first issue is the choice of calculating the geometric mean versus the arithmetic mean for the GND density. The choice of using the geometric mean is based on the established literature by Jiang et al. [47]. In addition, as shown in Fig. 13a of Appendix D, no significant difference exists between the geometric mean and the arithmetic mean for the data set examined here. Second, the value of the geometric mean reported here was determined ignoring those measurements that fell below the noise floor. The typical measurement of the EBSD data resulted in ~0.1% of the data falling below the noise floor. One might argue that eliminating these undetermined points artificially raises the GND values. However, if these data points are replaced by GND values even 5 orders of magnitude below the noise floor, the values for the geometric mean are statistically unchanged due to the very small fraction of these data points: see Figure 13b in Appendix D for illustration.

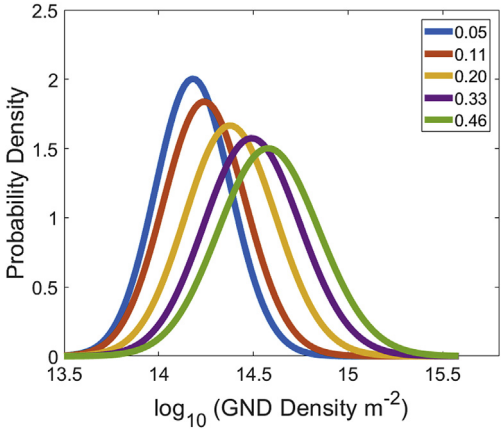

Fig. 6. Log-normal probability distribution of GND density for increasing compressive plastic strain 0.05, 0.11, 0.20, 0.33, and 0.46 for nickel samples.

4.2. Estimated total dislocation density and statistically stored dislocation density

During the compression of the nickel samples, the value of flow stress increases from 289 MPa to 679 MPa with increasing plastic strain due to work hardening. The measurement uncertainties associated with flow stress and plastic strain are below 1% and 0.5%, respectively; error bars are therefore not included in the plot. The flow stress corresponding to each plastic strain is determined by dividing the maximum load from the load-displacement curve by the current cross-sectional area of the compressed sample. The flow stress is plotted in Fig. 8a, showing significant work hardening at higher plastic strains and characteristic parabolic shape. Using Taylor's hardening model, it is straight-forward to estimate the total dislocation density responsible for the hardening of the material (assumes $\lambda_G = 30\mu m$ for the current nickel material), plotted

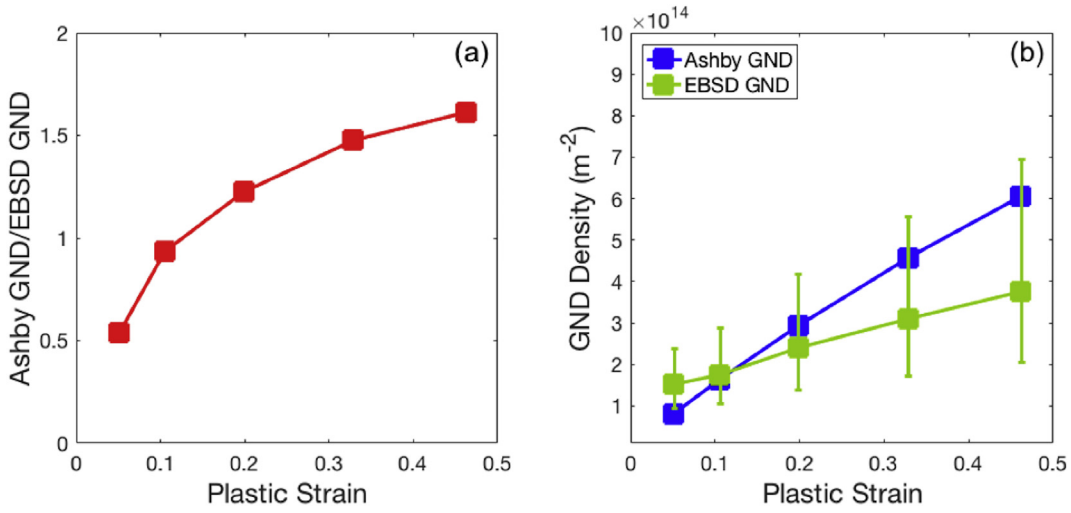

Fig. 7. (a) Ratio of predicted and measured GND density as a function of plastic strain, and (b) Measured GND density using EBSD based method plotted in blue line and predicted GND density according to Ashby's model plotted in green line with respect to plastic strain. The error bars plotted on the measured EBSD GND data are defined in the text. (For interpretation of the references to colour in this figure legend, the reader is referred to the Web version of this article.)

in Fig. 8b. The total dislocation density present increases from ~2.36×10^{14} to ~1.3×10^{15} m^{-2} as the imposed strain increases from 0.05 to 0.46, consistent with the higher flow stress required to deform it. The uncertainty of the calculated total dislocation density is around 2%. However, this uncertainty is based on the unknown error for c in the Taylor's work hardening. More work is needed to systematically evaluate the value for c in order to understand the exact contribution of different dislocation types and interactions, which will provide foundation for a more realistic estimate of the error of total dislocation density.

The estimated total dislocation density can be plotted together with the measured GND density, see Fig. 9 (dislocation density data is listed in Table 1). At 0.05 plastic strain, the GND density and the total dislocation density are of the same magnitude. However, the difference between the two, starts to become notable at higher plastic strains. This suggests that the primary contributor to strength of nickel is initially the geometrically necessary dislocations at small strains, concentrating near hot spots such as grain boundaries and triple junctions as shown in Fig. 10 (b, d, f). The GND distribution is illustrated in Fig. 9, Stage I. As the plastic strain increases, GND content increases steadily in hot spots and forms GNDs that divide the grain into differently oriented sub-structures i.e. kink bands as shown Fig. 10h and transit into the similarly oriented neighboring grain. At the same time, the fraction of statistically stored dislocations increases considerably from ~8.37×10^{13} to ~9.27×10^{14} m^{-2} to form dislocation cell microstructures and eventually outnumbers the GNDs, see Fig. 9 for Stage II and Stage III. The difference of the total dislocation density and GND density is an estimate of the SSD density, which is plotted as the red curve in Fig. 9. The distribution of SSDs in Fig. 9 is plotted based on the estimated density as well as knowledge of them being formed randomly into cell structures at higher plastic strains. Further investigation suggests that the SSD density outnumbers GND density at approx. 0.09 plastic strain; SSDs becomes the primary contributor above 0.09 plastic strain (for $\lambda_G = 30\mu m$). In Fig. 9, it can also be found that the SSD density is heavily dependent on the degree of deformation with a faster rate of change as a function of plastic strain, whereas GND density is weakly dependent on the deformation history as indicated by the flat green line. This result is in accordance with Ashby's prediction that SSD density varies

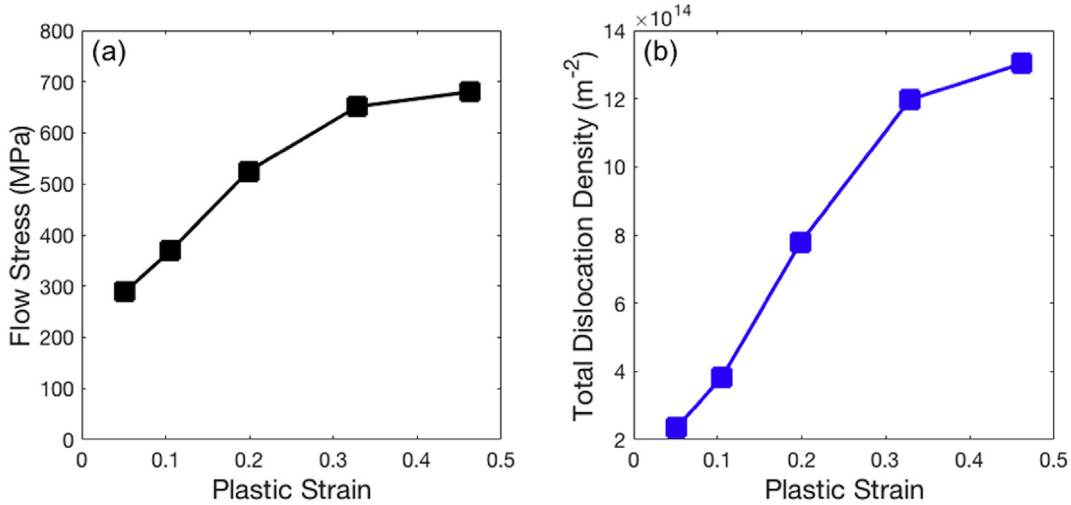

Fig. 8. (a) Compressive flow stress for maintaining the plasticity at different plastic strain for quasi-statically compressed pure nickel; (b) Total dislocation density estimated based on Taylor's hardening model and plotted against the corresponding plastic strains.

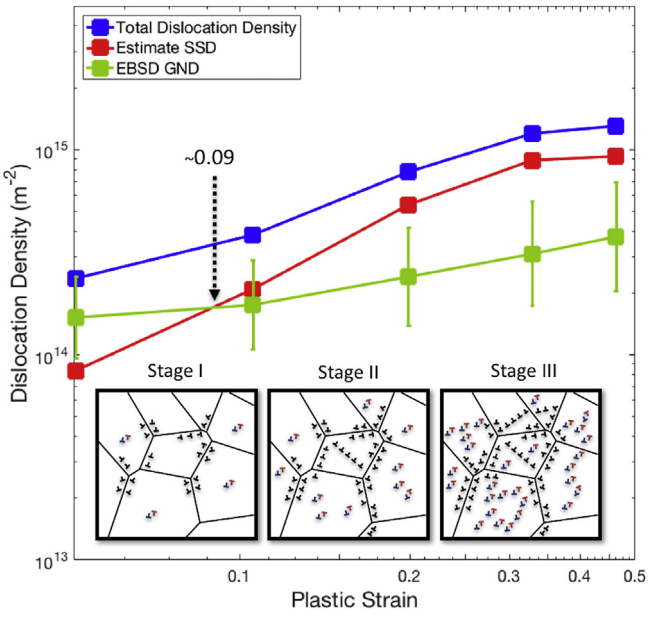

Fig. 9. Estimated total dislocation density from Taylor's model (blue), EBSD measured GND density (green) and, the difference of the two, the estimated SSD density (red), plotted with respect to corresponding plastic strains. Schematic diagrams of three stages of work hardening are plotted assuming the morphology of grains stay unchanged for illustration purpose, where the black ⊥ represents GND and each pair of blue and red ⊥ represent SSDs. (For interpretation of the references to colour in this figure legend, the reader is referred to the Web version of this article.)

nearly proportional to shear strain squared, but the GND density is linearly proportional to shear strain, therefore the GNDs will eventually be outnumbered by SSDs at higher plastic strains. The reason why GND density is higher initially may be due to rapid non-linear evolution of GNDs from unstrained state, therefore the validity of the Ashby's model at low strains is still unclear and is likely to be inaccurate. GND density calculation on a fully annealed sample using Hough based EBSD results in a large fraction of pixels near and below the noise floor, which implies a statistical average at least near or below the noise floor. However, data points below the noise floor are routinely removed to eliminate the measurement noise, which will significantly bias the GND density data distribution. Statistically robust analysis of unstrained sample is subject to future work using HR-EBSD.

5. Discussion

The Hough based EBSD technique has been proven to be a reliable method to extract GND density by many previous studies [30,34,35,38,39]. In this study, the measured GND density is comparable to Ashby's model prediction in Fig. 7b, being linearly dependent on the plastic strain within the range between 0.05 and 0.46. However, the differences are greatest at larger strains because Ashby's model is based on a simplified, homogeneous description of plastic deformation within materials. The nickel sample used in this study contains annealing twins and a heterogeneous grain size distribution, which leads to a broad spectrum of GND networks. In other words, the prediction made by Ashby for GND density, assuming GNDs are predominantly present along the grain boundaries, could serve as an estimate for the high density GND networks measured in EBSD. Nevertheless, Ashby's prediction does not accurately capture the low-density structures, which reduces the geometric mean of measured GND density at higher plastic strains. Work done by Jiang *et al.* [47] shows that the average GND density does vary with D^{-1} (D is the grain diameter) due to grain boundary hardening, but only at small strains (below 0.06), in agreement with the edge dislocation originated from the grain boundaries by Li *et al.* [55]. Values predicted from Ashby's model may not be valid for high strain samples. Physically, the breakdown of Ashby's model at higher strains could be attributed to the change in the aspect ratio of grains due to deformation, which could affect

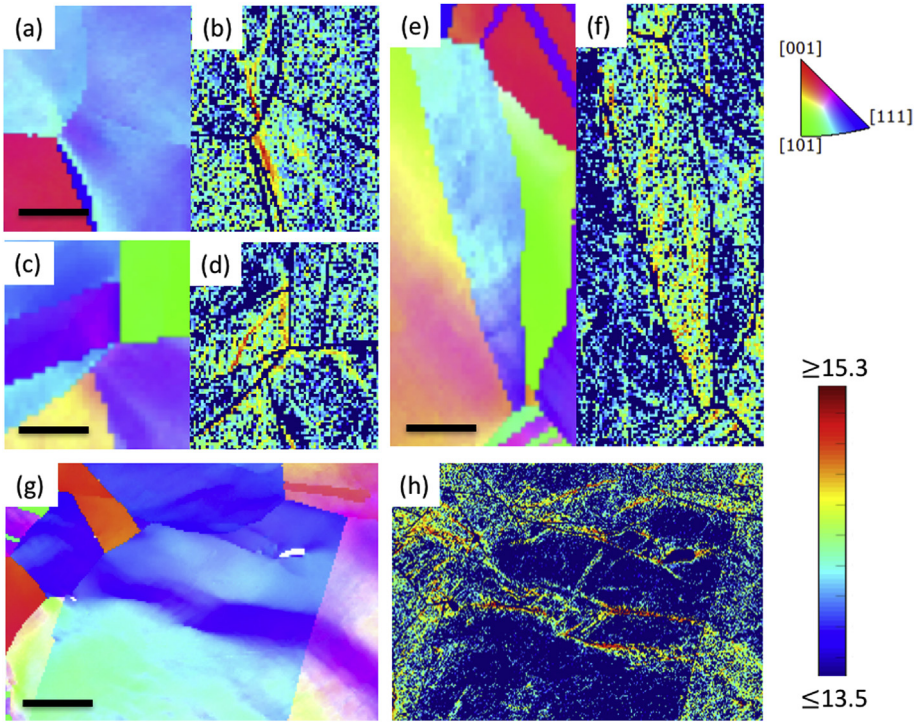

Fig. 10. (a), (c) and (e) are cropped EBSD images for 0.05 plastic strain sample and (g) is a selected area from 0.1 plastic strain sample; Examples of GND hot spots are found (b) near triple junction, (d) twin boundary, (f) across the thin tip of a grain and (h) kink band transition across grain boundary. Black bar is a 10 μm scale bar.

the value of 'actual' slip distance or potentially storage of energy due to configurational substructure evolution in the material over increasing random dislocation tangles [11,18,19]. Moreover, complex dislocation interactions with the deformed microstructure and other existing dislocations could also significantly influence the formation of GNDs, which is not included in Ashby's model. Modification of Ashby's original model is required in order to adapt it to more realistic microstructures, their evolution with increasing plastic strain, and higher strain scenarios. Future study is also required to investigate the evolution of GNDs at extremely low strain between 0 and 0.05 with advanced technique such as HR-EBSD. However, the challenge is that the reasonable range of interrogation length scale and limited angular resolution in measurement of GND density yields an inherent lower bound solution of the measured GND density [22], which might bias the result. For heavily deformed samples >0.05 strain, the fraction of pixels filtered below noise floor is insignificant to have any effect on the statistical analysis.

From Taylor's hardening model, work hardening is a result of the complex interaction of stored SSDs and GNDs. In our study, the flow stress of nickel is used to estimate the total dislocation density following Taylor's model, given that the friction stress for a high stacking fault energy FCC crystal, such as Cu and Ni, is negligible. However, the friction stress for BCC or other lower symmetry crystals is much higher and would, therefore, need to be included. With the GND density calculated, it is possible to estimate the SSD density at each plastic strain, enabling direct comparison of GND and SSD density as a function of plastic strain. Surely, the accuracy of the estimated SSD density will depend heavily on the accuracy of both total dislocation density and GND density. The uncertainty for total dislocation density is below 2% and the GND density is significantly higher than the noise floor (2.8×10^{13} m^{-2}), providing high confidence in the accurate determination of SSD density. Moreover, the parameters for the EBSD scan, such as step size, will also have an effect on the magnitude and distribution of GND density. An optimal step size of 500 nm has been chosen in this study, which is known to be small enough to reveal dislocation cells and large enough to save scan/computation time. A detailed explanation of the choice of step size can be found in the review by Wright [25]. Since compression of materials is non-uniform in the transverse direction, the scanned areas in our study are chosen to be near the center of the sample, where most plasticity resides, and away from the top and bottom surfaces, where deformation may be more constrained. In addition, the scanned area is almost 1 mm^2 covering a significant fraction of the deformed cross-sectional area. This provides robust statistics to our analysis for measured GND density.

This study has reached the conclusion that both GNDs and SSDs play an important role in the hardening of nickel, but predominate at different stages of work hardening. In the early stage of deformation, i.e. below 0.09 plastic strain in this case ($\lambda_G = 30\mu$m), the dislocations are predominantly GNDs due to presence of grain boundaries. As the measured GND density slowly increases in the lattice, the interaction of these dislocations leads to formation of greater numbers of SSDs. Since the multiplication of SSDs occurs at a much faster rate, SSDs are present in larger number than GNDs above 0.09 plastic strain ($\lambda_G = 30\mu$m), thus providing a more significant contribution to sample hardening. These results are in accordance with Ashby's theoretical analysis for copper in Fig. 4, where the yellow region of SSD density intersects the green line ($\lambda_G = 30\mu$m) at around 0.1 plastic strain, similar to what this study has found (0.09) in Fig. 9 for nickel. Direct comparison of two different materials is rationalized by the fact that copper and nickel are similar in terms of crystal structure, friction stress, and lattice parameter. The agreement between theory and experiment suggests SSD density measured in this study is of some significance. Although the measurement is an indirect technique, this study shows that it is a reasonable approach, and provides significant insight into the mechanisms controlling hardening of nickel. Most importantly, in addition to providing some experimental validation of Ashby's theory [3], this approach may serve as a useful tool in the future to explore many more aspects of deformation mechanisms for other metals and alloys across different strain rates, stress states, and temperatures.

6. Conclusions

The EBSD based GND density calculation enables us to explore the SSD density by subtracting the measured GND density from the estimated total dislocation density according to Taylor's hardening model. It enables a comprehensive study of the evolution of SSDs and GNDs for a quasi-statically compressed pure nickel sample at ambient temperature. In this study on nickel, it has been found that:

i) The measured GND density varies linearly from $\sim 1.52 \times 10^{14}$ to ~3.76×10^{14} m^{-2} with respect to plastic strain values ranging from 0.05 to 0.46. The linearity agrees with Ashby's model prediction in the strain range between 0.05 and 0.46; however, the magnitude of predicted GND density is, in general, an upper bound estimate to the high-density structures of measured GND density.
ii) From Taylor's hardening model, the total dislocation density for pure nickel has been determined to range from ~2.36×10^{14} to ~1.3×10^{15} m^{-2}, corresponding to a flow stress of 289 MPa–679 MPa. The significant rise in the total dislocation density is a result of rapid multiplication of SSDs from ~8.4×10^{13} to ~9.3×10^{15} m^{-2}, as a function of plastic strain.
iii) The majority of dislocations are GNDs for nickel (λ_G=30 μm) below 0.09 plastic strain, but GNDs are later outnumbered by SSDs above 0.09 plastic strain because of rapid non-linear multiplication of SSDs. Therefore, GNDs are responsible for the strengthening in nickel or other alloys at small deformation, whereas strength due to work hardening at large deformation is predominantly due to SSDs.

Acknowledgements

Los Alamos National Laboratory(LANL) is operated by Los Alamos National Security, LLC, for the National Nuclear Security Administration of the U.S. Department of Energy under contract DE-AC52-06NA25396. This work was partially sponsored by the Joint DoD/DOE Munitions Technology Development Program and the Dynamic Materials Science Campaign at LANL.

Appendix A. Lattice orientation gradient

The formal definition of the Nye tensor includes both the symmetric elastic strain distortion and the antisymmetric rotational distortion. Since the elastic strain is negligibly small, the Nye tensor[1] is equated to the curl of lattice rotation tensor.

$$\alpha_{ik} = \varepsilon_{jlk}\beta^{el}_{ij,l} \approx \varepsilon_{jlk}\omega_{ij,l} \tag{A1}$$

where $\boldsymbol{\omega}$ represents the small rigid body rotations of the lattice i.e. lattice rotation tensor.

[1] Kröner tensor is the transpose of the original Nye tensor $\boldsymbol{\alpha_{Kr\bar{o}ner} = \alpha^{T}_{Nye}}$, which switches the more commonly used ij subscripts on $\boldsymbol{\beta}$.

Suppose a finite rotation of $\Delta\varnothing$ is a rotation about rotation axis vector **m** by angle θ [56]. This effectively takes the lattice orientation at one point to the neighboring lattice orientation point.

$$\Delta\varnothing_{ij} = \delta_{ij}\cos\theta - \varepsilon_{ijk}m_k\sin\theta + (1-\cos\theta)m_i m_j \tag{A2}$$

$$\Delta\varnothing_{ij} \approx \delta_{ij} - \varepsilon_{ijk}m_k\theta \ (\theta \ is \ small) \tag{A3}$$

By definition, the lattice rotation tensor is related to the lattice rotation vector as:

$$\omega_{ij} = -\varepsilon_{ijk}\theta_k \tag{A4}$$

where $\theta_k = m_k\theta$. Hence, we can relate the lattice rotation tensor to the rotation matrix simply as:

$$\omega_{ij} = \Delta\varnothing_{ij} - \delta_{ij} \tag{A5}$$

Given the lattice orientation matrices of two neighboring points, the disorientation matrix can be readily obtained $\Delta\varnothing = g_B g_A^{-1}$ considering all the symmetry operators. Therefore, the lattice orientation gradients can be derived as:

$$\Delta\varnothing_{,l} = \frac{\Delta\varnothing - I}{d_l} = \frac{g_B g_A^{-1} - I}{d_l} \tag{A6}$$

Appendix B. Reference frame

According to Wheeler et al., the reference frames of Nye tensor can be defined in different ways [57]. It is therefore important to be consistent with what reference frames are used when the Nye dislocation tensor is decomposed into dislocation configurations. For instance, if the dislocation tensor relates the sample frame (subscripted in Greek letters) to the crystal frame (subscripted in Latin letters), the surface integral of the Nye dislocation tensor in the sample frame yields the local Burgers vector in the crystal frame.

$$\mathrm{B}_i = \oint\!\!\!\oint \alpha_{i\gamma} dS_\gamma \tag{B1}$$

In total, there are four equivalent variants of Nye dislocation tensors for different reference frames [31]. By pre- and/or post-multiplication with the (inverse) orientation tensor, the dislocation tensor can be transformed to different set of reference frames. In this study, the differentiation inside the curl of the disorientation field in the sample frame conflicts with the varying crystal frame associated with the disorientation field, which is remedied by aligning the disorientation field towards the sample frame. The resultant Nye dislocation tensor then relates the closure failure in the sample frame to the disorientation gradient in the sample frame, which could subsequently be transformed back to the crystal frame. Then, the dislocation configurations in Eq. (4) are in the same reference frame as the Nye tensor while using the Frank's loop construction, maintaining the consistency for use of reference frames. However, the disadvantage of taking the curl of the disorientation field demands interpolation at an off-grid point, which is ignored in this study. Fortunately, the error is negligibly small because only first-neighbors are used for calculating the disorientation matrix.

Appendix C

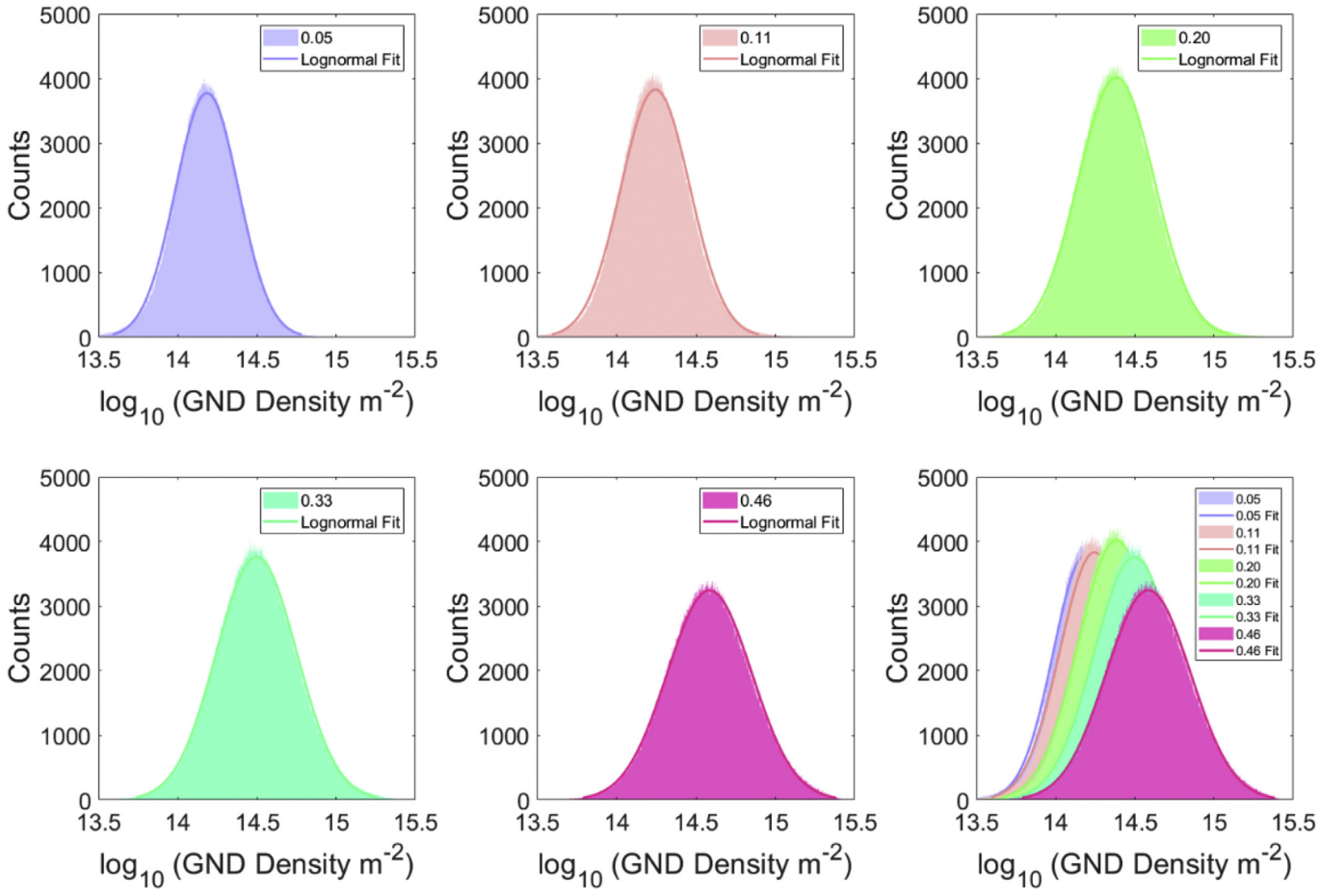

Fig. 11. : The actual GND density distribution data in logarithmic scale fitted with lognormal curves.

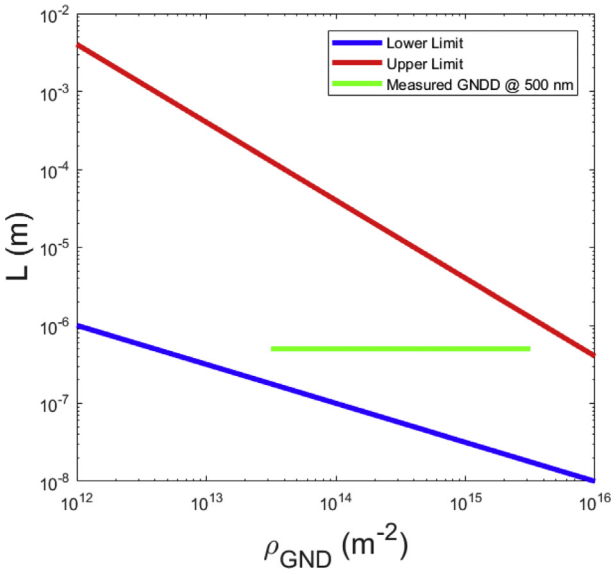

Fig. 12. Step size validation for use of GND density characterization.

Appendix D

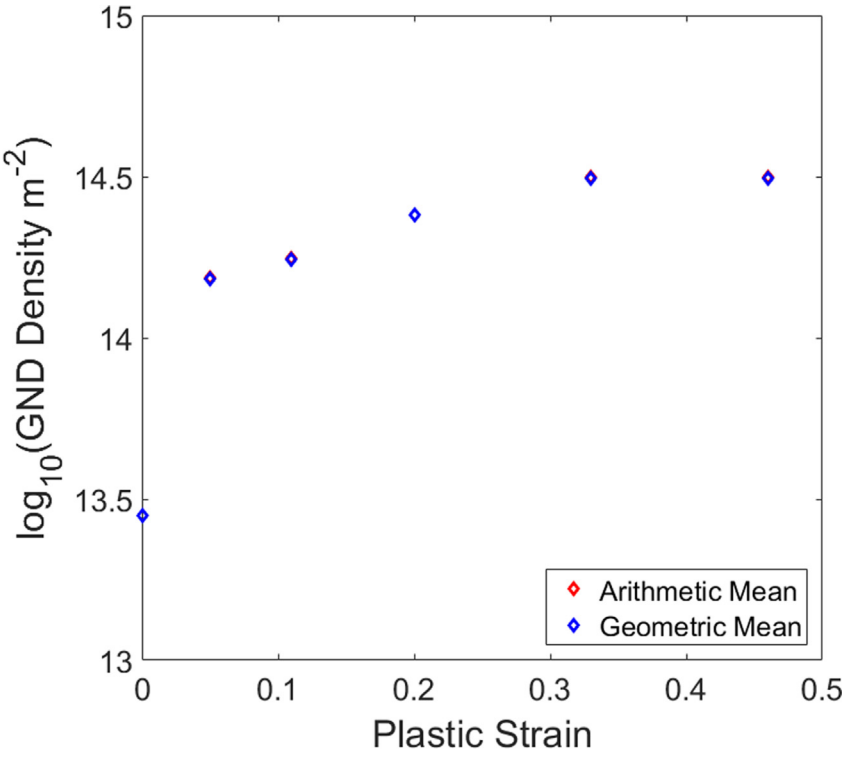

Fig. 13a. Plot comparing the GND density as determined by the geometric mean versus the arithmetic mean showing no significant difference in the results. The preference for using the geometric mean is based on previous work by Jiang et al. [J. Jiang, T. Britton, A. Wilkinson, Evolution of dislocation density distributions in copper during tensile deformation, Acta Materialia 61(19) (2013) 7227–7239.].

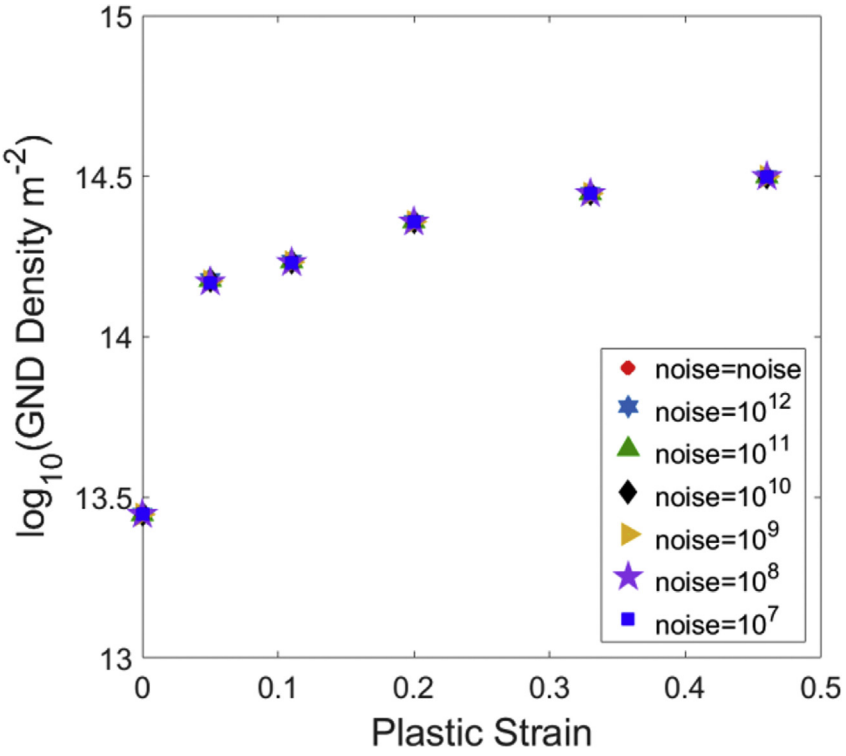

Fig. 13b. Plot comparing the GND density determined by the geometric mean where in the data for those measurement that were determined to be below the noise floor have been set to different low-density values from the noise floor itself down to 10^-7 in one order of magnitude step. For a typical measurement, the number of data point below the noise floor was on the order of 0.1%. As shown in the plot even values 5 orders of magnitude below the noise floor do not significantly alter the value of the geometric means determined in this study.

Table 1
Dislocation Density Data.

Plastic Strain	Ashby GND (m^{-2})	EBSD GND (m^{-2})	Total Dislocation (m^{-2})	SSD (m^{-2})
0.05	8.19×10^{13}	1.52×10^{14}	2.36×10^{14}	8.37×10^{13}
0.11	1.64×10^{14}	1.75×10^{14}	3.84×10^{14}	2.09×10^{14}
0.20	2.94×10^{14}	2.40×10^{14}	7.78×10^{14}	5.38×10^{14}
0.33	4.57×10^{14}	3.10×10^{14}	1.20×10^{15}	8.87×10^{14}
0.46	6.06×10^{14}	3.76×10^{14}	1.30×10^{15}	9.27×10^{14}

References

[1] M.A. Meyers, K.K. Chawla, Mechanical Behavior of Materials, Cambridge University Press Cambridge, 2009.
[2] D. Hull, D.J. Bacon, Introduction to Dislocations, 5 ed., Elsevier, 2011.
[3] W. Cai, W.D. Nix, Imperfections in Crystalline Solids, Cambridge University Press, 2016.
[4] N. Hansen, Polycrystalline strengthening, Metallurgical Transactions A 16 (12) (1985) 2167–2190.
[5] M. Ashby, The deformation of plastically non-homogeneous materials, Phil. Mag. 21 (170) (1970) 399–424.
[6] G.T. Gray III, S.R. Chen, K.S. Vecchio, Influence of grain size on the constitutive response and substructure evolution of MONEL 400, Metall. Mater. Trans. 30 (5) (1999) 1235–1247.
[7] D. Kuhlmann-Wilsdorf, N. Hansen, Geometrically necessary, incidental and subgrain boundaries, Scripta Metall. Mater. 25 (7) (1991) 1557–1562.
[8] H. Mughrabi, R. Wang, N. Hansen, A. Horsewell, T. Leffers, H. Lilholt, Deformation of polycrystals: mechanisms and microstructures, in: N. Hansen, A. Horsewell, T. Leffers, H. Lilholt (Eds.), Proc. 2nd Risø Int. Symp. On Metallurgy and Materials Science, Risø National Laboratory, Roskilde, Denmark, 1981, pp. 87–98.
[9] D. Hughes, Microstructure evolution, slip patterns and flow stress, Mater. Sci. Eng. 319 (2001) 46–54.
[10] D. Hughes, N. Hansen, Graded nanostructures produced by sliding and exhibiting universal behavior, Phys. Rev. Lett. 87 (13) (2001) 135503.
[11] B. Bay, N. Hansen, D. Kuhlmann-Wilsdorf, Deformation structures in lightly rolled pure aluminium, Mater. Sci. Eng. 113 (1989) 385–397.
[12] F. Frank, Report of the Symposium on the Plastic Deformation of Crystalline Solids, Carnegie Institute of Technology, Pittsburgh, 1950, pp. 150–154.
[13] J. Hirth, D. Barkett, J. Lothe, Stress fields of dislocation arrays at interfaces in bicrystals, Philos. Mag. a 40 (1) (1979) 39–47.
[14] J.F. Nye, Some geometrical relations in dislocated crystals, Acta Metall. Mater. 1 (2) (1953) 153–162.
[15] M. Rashid, G.T. Gray III, S. Nemat-Nasser, Heterogeneous deformations in copper single crystals at high and low strain rates, Philosophical Magazine A 65 (3) (1992) 707–735.
[16] U. Kocks, A statistical theory of flow stress and work-hardening, Philosophical Magazine 13 (123) (1966) 541–566.
[17] O. Rezvanian, M. Zikry, A. Rajendran, Statistically stored, geometrically necessary and grain boundary dislocation densities: microstructural representation and modelling, Proc. Roy. Soc. Lond. A: Math. Phys. Eng. Sci. Roy. Soc. (2007) 2833–2853.
[18] D. Kuhlmann-Wilsdorf, Theory of plastic deformation:-properties of low energy dislocation structures, Mater. Sci. Eng. 113 (1989) 1–41.
[19] D.A. Hughes, N. Hansen, Deformation structures developing on fine scales, Phil. Mag. 83 (31–34) (2003) 3871–3893.
[20] J. Huang, G.T. Gray III, Microband formation in shock-loaded and quasi-statically deformed metals, Acta Metall. Mater. 37 (12) (1989) 3335–3347.
[21] J. Jiang, T.B. Britton, A.J. Wilkinson, Measurement of geometrically necessary dislocation density with high resolution electron backscatter diffraction: effects of detector binning and step size, Ultramicroscopy 125 (2013) 1–9.
[22] J. Kysar, Y. Saito, M. Oztop, D. Lee, W. Huh, Experimental lower bounds on geometrically necessary dislocation density, Int. J. Plast. 26 (8) (2010) 1097–1123.

[23] D. Dingley, M. Longden, J. Weinbren, J. Alderman, Online analysis of electron back scatter diffraction patterns. 1. Texture analysis of zone refined polysilicon, Scanning Microsc. 1 (2) (1987) 451–456.
[24] B.L. Adams, S.I. Wright, K. Kunze, Orientation imaging: the emergence of a new microscopy, Metall. Mater. Trans. 24 (4) (1993) 819–831.
[25] S.I. Wright, A review of automated orientation imaging microscopy(OIM), J. Comput. Assist. Microsc. 5 (3) (1993) 207–221.
[26] M. Meisnar, A. Vilalta-Clemente, M. Moody, K. Arioka, S. Lozano-Perez, A mechanistic study of the temperature dependence of the stress corrosion crack growth rate in SUS316 stainless steels exposed to PWR primary water, Acta Mater. 114 (2016) 15–24.
[27] I. Ghamarian, Y. Liu, P. Samimi, P.C. Collins, Development and application of a novel precession electron diffraction technique to quantify and map deformation structures in highly deformed materials-as applied to ultrafine-grained titanium, Acta Mater. 79 (2014) 203–215.
[28] W. Pantleon, Resolving the geometrically necessary dislocation content by conventional electron backscattering diffraction, Scripta Mater. 58 (11) (2008) 994–997.
[29] S. Zaefferer, S. Wright, D. Raabe, 3D-orientation microscopy in a FIB SEM: a new dimension of microstructure characterization, Microsc. Microanal. 13 (S02) (2007) 1508.
[30] M. Calcagnotto, D. Ponge, E. Demir, D. Raabe, Orientation gradients and geometrically necessary dislocations in ultrafine grained dual-phase steels studied by 2D and 3D EBSD, Mater. Sci. Eng. 527 (10) (2010) 2738–2746.
[31] P.J. Konijnenberg, S. Zaefferer, D. Raabe, Assessment of geometrically necessary dislocation levels derived by 3D EBSD, Acta Mater. 99 (2015) 402–414.
[32] M.E. Fitzpatrick, A. Lodini, Analysis of Residual Stress by Diffraction Using Neutron and Synchrotron Radiation, CRC Press, 2003.
[33] B.C. Larson, A. El-Azab, W. Yang, J.Z. Tischler, W. Liu, G.E. Ice, Experimental characterization of the mesoscale dislocation density tensor, Phil. Mag. 87 (8–9) (2007) 1327–1347.
[34] C. Zhu, V. Livescu, T. Harrington, O. Dippo, G.T. Gray III, K.S. Vecchio, Investigation of the shear response and geometrically necessary dislocation densities in shear localization in high-purity titanium, Int. J. Plast. 92 (2017) 148–163.
[35] C. Zhu, T. Harrington, V. Livescu, G.T. Gray III, K.S. Vecchio, Determination of geometrically necessary dislocations in large shear strain localization in aluminum, Acta Mater. 118 (2016) 383–394.
[36] A.J. Wilkinson, D. Randman, Determination of elastic strain fields and geometrically necessary dislocation distributions near nanoindents using electron back scatter diffraction, Phil. Mag. 90 (9) (2010) 1159–1177.
[37] T. Britton, A. Wilkinson, High resolution electron backscatter diffraction measurements of elastic strain variations in the presence of larger lattice rotations, Ultramicroscopy 114 (2012) 82–95.
[38] E. Demir, D. Raabe, N. Zaafarani, S. Zaefferer, Investigation of the indentation size effect through the measurement of the geometrically necessary dislocations beneath small indents of different depths using EBSD tomography, Acta Mater. 57 (2) (2009) 559–569.
[39] Y. Guo, D.M. Collins, E. Tarleton, F. Hofmann, J.Z. Tischler, W. Liu, R. Xu, A.J. Wilkinson, T.B. Britton, Measurements of stress fields near a grain boundary: exploring block arrays of dislocations in 3D, Acta Mater. 96 (1 September 2015) 229–236. https://doi.org/10.1016/j.actamat.2015.05.041.
[40] D. Yan, C.C. Tasan, D. Raabe, High resolution in situ mapping of microstrain and microstructure evolution reveals damage resistance criteria in dual phase steels, Acta Mater. 96 (2015) 399–409.
[41] J. Jiang, F.P. Dunne, T.B. Britton, Toward predictive understanding of fatigue crack nucleation in Ni-Based superalloys, Jom-Us 69 (5) (2017) 863–871.
[42] G. Speich, R. Fisher, Recrystallization, grain growth and textures, Am. Soc. Metals (1966) 563. Metals Park, Ohio.
[43] T.B. Britton, A.J. Wilkinson, Stress fields and geometrically necessary dislocation density distributions near the head of a blocked slip band, Acta Mater. 60 (16) (2012) 5773–5782.
[44] G.I. Taylor, Plastic strain in metals, J. Inst. Met. 62 (1938) 307–324.
[45] X. Qiu, Y. Huang, W. Nix, K. Hwang, H. Gao, Effect of intrinsic lattice resistance in strain gradient plasticity, Acta Mater. 49 (19) (2001) 3949–3958.
[46] L. Kubin, A. Mortensen, Geometrically necessary dislocations and strain-gradient plasticity: a few critical issues, Scripta Materialia 48 (2) (2003) 119–125.
[47] J. Jiang, T. Britton, A. Wilkinson, Evolution of dislocation density distributions in copper during tensile deformation, Acta Mater. 61 (19) (2013) 7227–7239.
[48] F.F. Lavrentev, The type of dislocation interaction as the factor determining work hardening, Mater. Sci. Eng. 46 (2) (1980) 191–208.
[49] R. Farraro, R.B. Mclellan, Temperature dependence of the Young's modulus and shear modulus of pure nickel, platinum, and molybdenum, Metall. Mater. Trans. 8 (10) (1977) 1563–1565.
[50] A.d.S. Scari, B.C. Pockszevnicki, J. Landre Junior, P.A.A. Magalhaes Junior, Stress-strain compression of AA6082-T6 aluminum alloy at room temperature, Journal of Structures 2014 (2014).
[51] S.I. Wright, M.M. Nowell, D.P. Field, A review of strain analysis using electron backscatter diffraction, Microsc. Microanal. 17 (3) (2011) 316–329.
[52] D. Hughes, D. Chrzan, Q. Liu, N. Hansen, Scaling of misorientation angle distributions, Phys. Rev. Lett. 81 (21) (1998) 4664.
[53] M. Kamaya, A.J. Wilkinson, J.M. Titchmarsh, Quantification of plastic strain of stainless steel and nickel alloy by electron backscatter diffraction, Acta Mater. 54 (2) (2006) 539–548.
[54] B.L.K. Thomas, Geometric means and measures of dispersion, Biometrics 35 (4) (1979) 908–909.
[55] J.C. Li, Petch relation and grain boundary sources, Transactions of the Metallurgical Society of AIME 227 (1) (1963), 239-&.
[56] S. Sun, B. Adams, W. King, Observations of lattice curvature near the interface of a deformed aluminium bicrystal, Philos. Mag. a 80 (1) (2000) 9–25.
[57] J. Wheeler, E. Mariani, S. Piazolo, D. Prior, P. Trimby, M. Drury, The weighted Burgers vector: a new quantity for constraining dislocation densities and types using electron backscatter diffraction on 2D sections through crystalline materials, J. Microsc. (Oxf.) 233 (3) (2009) 482–494.
[58] F. Bachmann, R. Hielscher, H. Schaeben, Texture analysis with MTEX–free and open source software toolbox, Solid State Phenom. 160 (2010) 63–68.